CHALMERS
UNIVERSITY OF TECHNOLOGY

Effects of Morphological Variations on Hemodynamic Parameters in the Middle Cerebral Artery

A study conducted through Computational Fluid Dynamics

Bachelor thesis in Mechanics and Maritime Sciences

PONTUS MALMSKÖLD
JOHANNA ODBRATT
EHSAN PEYVANDI
LOUISE ÅKESSON

DEPARTMENT OF
MECHANICS AND MARITIME SCIENCES

CHALMERS UNIVERSITY OF TECHNOLOGY
Gothenburg, Sweden 2022
www.chalmers.se

BACHELOR THESIS 2022:05

Effects of Morphological Variations on Hemodynamic Parameters in the Middle Cerebral Artery

A study conducted through Computational Fluid Dynamics
Bachelor thesis in Mechanics and Maritime Sciences

PONTUS MALMSKÖLD
JOHANNA ODBRATT
EHSAN PEYVANDI
LOUISE ÅKESSON

Department of Mechanics and Maritime Sciences
Division of Fluid Dynamics
CHALMERS UNIVERSITY OF TECHNOLOGY
Gothenburg, Sweden 2022

Effects of Morphological Variations on Hemodynamic Parameters in the Middle Cerebral Artery
A study conducted through Computational Fluid Dynamics

PONTUS MALMSKÖLD
JOHANNA ODBRATT
EHSAN PEYVANDI
LOUISE ÅKESSON

Bachelor Thesis 2022:05
Department of Mechanics and Maritime Sciences
Chalmers University of Technology
SE-412 96 Gothenburg
Sweden
Telephone: + 46 (0)31-772 1000

Cover:
Reconstruction of the cerebral circulation system of patient 27

Printing /Department of Mechanics and Maritime Sciences
Gothenburg, Sweden 2022

Abstract

Stroke is a large contributor to deaths around the world. One common cause of stroke is an Intracranial Aneurysm, which causes the wall of the artery to expand and potentially rupture leading to hemorrhage in the brain. The formation and rupture of both aneurysms as well as other contributors to stroke, are tied to specific hemodynamic properties such as wall shear stress. This paper aims to investigate the differences in wall shear stress in different patients in a bifurcating part of the cerebral vascular system that is prone to developing stroke; the middle cerebral artery. This in order to see how morphological differences between patients affect the hemodynamic parameters such as wall shear stress. This was done using an *in silico* method within Computational fluid dynamics called the Lattice Boltzmann method for two different patients. The Herschel Bulkley model was used in order to properly model the non-Newtonian flow of blood. The data for the two patients were provided though open-source MRI scans where the vascular system was extracted through thresholding. The results of simulating the flow for both patients showed that the mean shear rate is quite similar for the two patients, with some significant differences in local shear rate. These differences were attributed to the bifurcation angles of the arteries, where the patient with the largest bifurcation angle had the highest local shear rate both in and after the bifurcation. A higher shear rate implies a higher wall shear stress, which resulted in the fact that a larger bifurcation angle seems to give rise to a higher wall shear stress. Hence, the risk of developing Intracranial Aneurysms and other conditions leading to stroke in the middle cerebral artery, seems to be higher when the bifurcation angle is large.

Sammanfattning

Stroke är en stor bidragande faktor till dödsfall världen över. En vanlig orsak till stroke är intrakraniellt pulsåderbråck, som orsakar en expansion och ett potentiellt bråck i en artär och leder till en blödning i hjärnan. Utvecklingen av såväl pulsåderbråck som andra bidragande faktorer till stroke, är kopplade till specifika hemodynamiska parametrar som exempelvis väggskjuvspänning. Syftet med denna studie är att undersöka skillnader i väggskjuvspänning för olika patienter i en förgrening för en del av det cerebrala vaskulära cirkulationssystemet som är benägen att utveckla stroke; den mellersta hjärnartären. Detta för att se hur morfologiska skillnader mellan patienter påverkar de hemodynamiska parametrarna såsom väggskjuvspänning. Detta har gjorts genom att använda en *in silico*-metod inom Computation fluid dynamics som heter Lattice Boltzmann-metoden, för två olika patienter. Herschel Bulkley-modellen användes sedan för att med större noggrannhet kunna modeller ett icke-newtonskt blodflöde. Datan för patienterna var tillgänlig via open-source i form av MR-bilder där det vaskulära systemet extraherades genom thresholding. Resultaten från simuleringarna av flödet visade att medelvärdet av skjuvhastigheten var relativt likt hos båda patienter, medan tydliga skillnader i den lokala skjuvhastigheten observerades. Dessa skillnader verkar främst bero på artärernas förgreningsvinklar, där patienten med med störst vinkel hade den högsta lokala skjuvhastigheten både i och efter förgreningen. En högre skjuvhastighet innebär i sin tur en högre väggskjuvspänning, vilket resulterade i att en större förgreningsvinkel verkade medföra en högre väggskjuvspänning. Detta tyder på att risken för att utveckla pulsåderbråck eller andra tillstånd som kan bidra till stroke i den mellersta hjärnartären, verkar öka då förgreningsvinkeln är stor.

Acknowledgement

We want to express our gratitude to our supervisor Dario Maggiolo for his time, assistance, advice, and the motivation he provided to us. We also want to thank Erik Lindgren for his guidance and advice about the biological aspects of the brain.

Contents

Nomenclature

Abbreviations

CFD Computational Fluid Dynamics

IA Intracranial aneurysm

LBM Lattice Boltzmann method

LB-units Lattice Boltzmann units

MCA Middle cerebral artery

N-S Navier- Stokes

RBC Red blood cells

WSS Wall Shear Stress

Parameters

ρ Density $[kg/m^3]$

p Pressure $[N/m^2]$

$\mathbf{V}$ Velocity vector $[m/s]$

v *with subscript* Velocity in arbitrary direction $[m/s]$

g Gravitational acceleration $[m/s^2]$

T Temperature $[K]$

τ shear stress $[N/m^2]$

$\dot{\gamma}$ shear rate $[s^{-1}]$

μ dynamic viscosity $[Ns/m^2]$

η Apparent viscosity $[Ns/m^2]$

k consistency $[Ns^n/m^2]$

n flow index $[-]$

τ_0 yield stress $[N/m^2]$

τ_{max} maximum shear stress in any direction $[N/m^2]$

M Stress growth exponent $[s]$

Re Reynolds number $[-]$

Bn Bingham number $[-]$

C Dimensionless consistency $[-]$

Ω_i Collision operator

f_i Density function

f_i^{eq} Equilibrium form of distribution function

$S_{\alpha\beta}$ Strain rate tensor

D_{II} 2nd invariant of the strain rate tensor

$\bar{\dot{\gamma}}$ Mean shear rate $[s^{-1}]$

Angles

α between superior and inferior

β between superior and main

γ between inferior and main

Superscripts

$*$ Dimensionless parameter

Subscripts

c characteristic parameter

LB parameter in Lattice Boltzmann units

1 Introduction

About 10% of all deaths in industrialised countries are caused by strokes. Stroke is a collective name for diseases caused by an internal bleeding in the brain, intracerebral hemorrhage, or a thrombus blocking the artieries. If not deadly, a stroke can cause severe damage to the patient and usually requires extensive aftercare and rehabilitation [1, 2]. Intracranial aneurysm (IA) is an example of a relatively common cerebrovascular condition that is especially prone to induce intracerebral hemorrhage. The condition causes the wall of an artery to expand, weaken and thereby creating a bubble-like structure; an aneurysm [3]. Consequently, the aneurysm is more vulnerable to rupturing and causing a stroke than the surrounding tissue.

The potential development of a stroke depends on a variety of factors including genetics, environmental and lifestyle factors as well as any underlying diseases. These factors can lead to major differences between patients in hemodynamic- and flow properties, meaning the physiological function of the circulation system, and in the vascular morphology [4]. The meaning of vascular morphology is the actual structure and form of the blood vessels [5], which as mentioned differs between different people. A clear example of where differentiations in morphology between people always exists, is the angles of where arteries and other vessels bifurcates into smaller branches. Hence, the study of cerebrovascular morphology, and more specifically the bifurcation angles, in relation to the development of stroke is highly relevant when it comes to risk assessment and prevention of stroke.

1.1 Background

In spite of the mentioned factors increasing the risk of getting a stroke, researchers have found that strokes are potentially preventable using the right tools and examining the flow characteristics of the blood [1]. Computational fluid dynamics (CFD), is a branch of fluid dynamics with numerical methods to model and analyze complex flows, and is frequently utilized in many industrial applications [6]. Lately however, CFD has furthermore proven to make prominent progress within the cardiovascular field as well, by using *in silico* methods to examine and assess the hemodynamic properties of the blood flow such as velocity, pressure, shear stress and shear rate [6, 7]. *In silico* is when a biological process or reaction occurs by the means of a computer [8], while in vivo studies on the other hand are made directly on the living organism [9]. Using *In silico* methods as oppose to *in vivo*, is a minimally-invasive assessment method since the physical interaction during the analysis is non existent.

One large branch of CFD is the Lattice Boltzmann method (LBM), which is used to obtain continuum flow quantities based on particle interactions. LBM is an incredibly versatile method that can be used in complex and multiscale flows [10]. By utilizing CFD and LBM to analyze the flow parameters in relation to MRI-scans of the cerebrovascular system, a better understanding on how the cerebrovascular morphology affects the risk of getting a stroke, can be obtained. Consequently, the possibilities of making progress with the preventive work of strokes increases profoundly. This could in turn lead to a reduction of the large amount of people that suffers from strokes worldwide.

1.2 Objective

The general objective of this study is to analyze whether or not CFD can be used to model and simulate the blood flow in the human cerebral circulation system with different morphological features. The simulations will be done on the middle cerebral artery (MCA) using the *in silico* Lattice Boltzmann method, for two patients with different sets of data. The blood will be modelled using both a Newtonian as well as a non-Newtonian approach. The objective is furthermore to investigate the correlation between the morphology of a certain patient's middle cerebral artery, and the flow parameters of the blood. Thus, the variations in the two patient's morphology will be analyzed in relation to the different simulation results and connected to the potential development of IA and other contributors to stroke. The main morphology of interest is the bifurcation angle of the MCA, in correlation to the magnitude of the wall shear stresses that the blood flow gives rise to.

1.3 Scope

The main focus of this study lies on proving the applicability and efficiency of using *in silico* methods for investigating the hemodynamics of the brain. Hence, the study will primarily be approached using a fluid dynamics point of view. The simulations will furthermore be analyzed in relation to the morphology of the two patient's arteries. This examination requires a base level of knowledge of biomechanical aspects such as blood properties, the MCA and how hemodynamics and flow properties affect the patient's cerebral circulation system and thereby their overall health.

The simulations will only be applied on the middle cerebral artery, which is chosen on the basis of two different reasons. The first reason is that the geometry of the artery is suitable with respect to the demands on the vessel set by the simulation environment. The other reason is that the MCA has a relatively high exposure to intracerebral hemorrhage and aneurysms, which increases the relevance of analyzing that specific artery.

Regarding the simulation, a few simplifications are made due to the high complexity of blood flows. The first limitation is that a steady state in- and out-flow is modelled instead of a pulsating flow. Furthermore, solid artery walls are used instead of elastic walls. The last limitation is that the flow will be treated as laminar.

2 Theory

In this chapter, relevant theory is introduced. The theory related to the biological aspects is presented first, followed by the theory treating the mechanical and computational parts.

2.1 Biological theory

In this section some essential biological terms and concepts are explained further. Firstly, the middle cerebral artery is accounted for, along with a description of how the morphology of the cerebral arteries can affect the flow parameters. Lastly, some current methods in the medical field of preventive work against strokes are explained.

2.1.1 Middle cerebral artery and its morphology

The middle cerebral artery is one of the major arteries supplying blood to the brain. The MCA is a branch of the internal carotid artery in the circle of willis, along with the slightly thinner branch named the anterior cerebral artery. The MCA itself is then divided into four parts, see Figure 1. The first part (M1) is called the sphenoidal or horizontal segment, and the second part (M2) is denoted as the insular segment. The two last parts (M3 and M4) are called the opercular and the cortical segment. The majority of the lateral surface of the hemisphere is supplied by the MCA. This part of the brain controls the motor and sensory areas excluding leg-, perineum-, auditory- and speech areas [11].

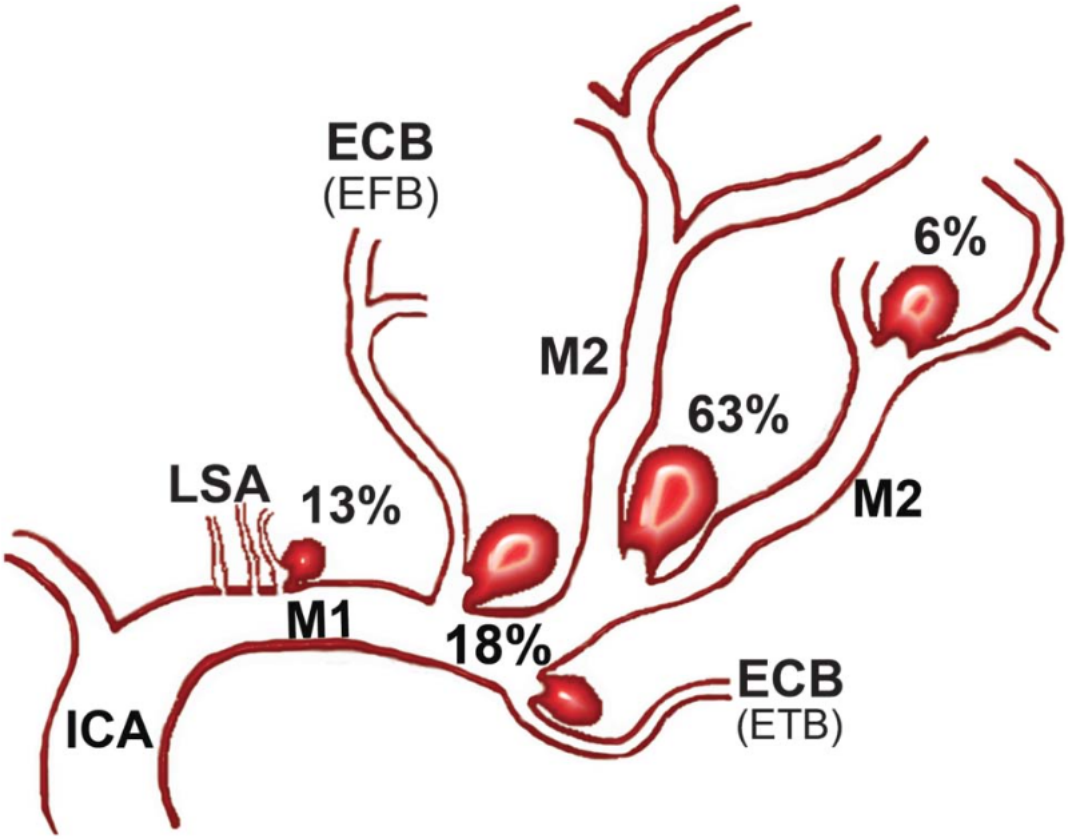

Figure 1: Middle cerebral artery divided into M1 and M2. This photo (https://operativeneurosurgery.com/lib/exe/detail.php?id=middle_cerebral_artery_m1_segment_aneurysm&media=middlecerebralarteryaneurysmlocalization.png) by Unknown Author is licensed under CC Attribution-Share Alike 4.0 International (https://creativecommons.org/licenses/by-sa/4.0/deed.en)

The MCA is an artery with a relatively high risk at developing for example intracerebral hemorrhage and other diagnoses classified as stroke. These conditions are initially caused by a high pressure on the walls of the artery, and thereby a high hemodynamic stress [15]. The MCA is one of the largest arteries supplying blood to the brain, which implies that it carries a high volume of blood. This makes it particularly vulnerable to changes in both the geometry as well as the flow parameters. Hence, the many bifurcations of the MCA are especially exposed to a high hemodynamic stress. This is due to the fact that the bifurcations causes the velocity of the blood flow to decrease rapidly, which in turn gives rise to an increased pressure and thereby a higher hemodynamic stress after the bifurcation [15, 16].

Regarding the morphology of the MCA, there are an infinite number of variants on how it can look like since each and every individual is unique. The first division of the main MCA however (M2)

is classified into three differents cases. The first and most common division is a bifurcation into a superior and an inferior part, which occurs for about 78% of the cases. For about 12% the MCA will instead be divided into three branches; a superior, a middle and an interior part through a trifurcation. For the last 10% it will be divided into many small branches [11]. As mentioned before, the bifurcations or trifurcations of the MCA affects the flow parameters of the blood such as pressure, shear stress and velocity. This fact has contributed to further research regarding the bifurcation angle, in order to determine how the angle affects the hemodynamic stress and consequently the risk of getting a stroke. Although the results are not unambiguous nor well established, some studies suggest that a larger bifurcation angle provides a higher hemodynamic stress and therefore a higher risk at developing for example IA [15, 17, 12].

2.1.2 Prevention of stroke

The middle cerebral artery is one of the most common pathologically affected blood vessel overall. Some of the most common pathologies are embolism, lenticulostriate infarct, arteriovenous malformations and aneurysm. Embolism is a blockage-causing piece of material which can cause a partial or total blockage of the blood flow. Lenticulostriate infarct is cerebral ischemia involving the territory supplied by the deep perforating branches of the middle cerebral artery. Arteriovenous Malformations are connections between the arteries and veins which are abnormal and entails a higher hemorrhage risk. For all of these diseases the vascular surgeons are challenged to decide whether or not to operate surgically. The variables describe rapid decision-making as a complex process that is strongly dependent on the vascular surgeon's experience and judgment.[13].

Regarding MCA aneurysms, microsurgical treatment is well established as the preferred surgical option to eliminate the aneruysm. Another option is endovascular treatment, where the benefits of using endovascular treatment over microsurgical treatment are particularly appealing to patients since the procedures are safe, do not impact the patient's appearance and are less intrusive. Furthermore, the majority of MCA aneurysms are difficult to reach and have broad-necked aneurysms with unfavorable dome-to-neck ratios, making them unsuitable for an endovascular approach[14].

2.2 Mechanical and computational theory

In this section the theory needed to understand the mechanical and computational part of this study is explained.

2.2.1 Image processing

Thresholding is a method of segmenting images where greyscale images are made into binary images. In an image acquired via MRI, different materials corresponds to different pixel intensities. The thresholding method is usually implemented by setting threshold constants, and discard pixels with intensity between the threshold constants. In that way only the desired materials will remain in the image[18].

2.2.2 Governing equations

Navier-Stokes (N-S) equations ,Equations 2 and 1, are based on the conservation of mass and momentum. N-S are used in CFD to give a differential relation for the momentum of, for example, an incompressible fluid [21, p. 211]. In Equation 2 $\mathbf{V}$ is the velocity vector of the flow field, ∇ indicates the gradient differential operator and ∇^2 is the laplace differential operator. On the right hand side of momentum equation, are sum of all forces that act on a fluid particle ($\mathbf{g}$ gravity, p pressure, and μ viscous forces) that leads to change of total momentum of the fluid particle on the left hand side of the equation.

$$Continuity: \quad \nabla \cdot \mathbf{V} = 0 \tag{1}$$

$$Momentum: \quad \rho \frac{D\mathbf{V}}{Dt} = \rho \mathbf{g} - \nabla p + \mu \nabla^2 \mathbf{V} \tag{2}$$

2.2.3 Flow properties of blood

Blood is made up of different kinds of blood cells. The shape of the cells leads the dynamic properties of blood to differ from Newtonian fluids, such as water. Blood is therefore considered a non-Newtonian fluid. It is mainly the shape of the red blood cells (RBC) that gives blood its dynamic properties. One of the properties that differentiates blood from a Newtonian fluid is its shear thinning behaviour [20]. Shear thinning means that the viscosity of the fluid decreases with higher shear rate (Equation 4). Since blood generally flows through circular arteries, the viscosity will be high in the center of the artery. The viscosity will be lower the closer the blood is to the artery walls, due to the aggregation of the RBC at the center of the artery

The behaviour of RBC are, as mentioned before, important for the blood's properties. Two important characteristics of RBC are that they are deformable and they can be aggregated. Deformability entails that they can change their shape to ellipsoidal structures which allows them to have a good streamlined which will decrease blood viscosity. The deformability has the greatest impact on the viscosity at high shear stress while the blood's ability to aggregate has greatest impact at low shear stress. When the RBC aggregate, they go to rouleaux structures which tend to increase the friction resistance between the flow lines and thereby raise the viscosity of the blood under low shear conditions. [19].

2.2.4 Non-Newtonian fluid models

In a Newtonian fluid, the shear rate has no effect on the viscosity of the fluid and the viscosity μ is constant. The shear stress τ in a Newtonian fluid can therefore be calculated according to Equation 3 [21, p. 22].

$$\tau = \mu \frac{du}{dy} \tag{3}$$

Fluids that do not follow the linear law of Equation 3 are called non-Newtonian fluids. Therefore, the calculation of shear stress τ should be in a way that the non-linearity of viscosity should be taken into account. To model the flow of blood, several models will be combined into what is known as the Herschel Bulkley Model with Papanastasiou Regularisation. The model and its different parts will be explained and elaborated upon in this chapter.

The constant viscosity in the Newtonian model will be replaced by an apparent viscosity $\eta(\dot{\gamma})$ that is dependent on the shear rate $\dot{\gamma}$ [22, p. 6]. $\dot{\gamma}$ and τ is calculated as:

$$\dot{\gamma} = \frac{\partial u}{\partial y} \tag{4}$$

$$\tau = \eta(\dot{\gamma})\dot{\gamma} \tag{5}$$

To draw a parallel to the Newtonian model, the shear stress would be $\tau = \eta(\dot{\gamma})\dot{\gamma}$ where $\eta(\dot{\gamma}) = \mu$.

To be able to model the shear thinning behaviour of blood the power-law model is used. The power-law model is a widely used non-Newtonian model that enables the fluid to exhibit both shear thinning and thickening behaviour [22, p. 7]. The power-law model is presented below:

$$\eta(\dot{\gamma}) = k|\dot{\gamma}|^{n-1} \tag{6}$$

Where n is the flow index and k is the consistency. n is used to model the shear thinning and thickening behaviour. When $n < 1$ the flow will be shear thinning and $n > 1$ gives a shear thickening behaviour. The power-law model gives that:

$$\text{Shear thinning, } n < 1 : \eta(0) = \infty \text{ and } \eta(\infty) = 0$$
$$\text{Shear thickening, } n > 1 : \eta(0) = 0 \text{ and } \eta(\infty) = \infty$$

Which is not physically reasonable as $\eta(0)$ and $\eta(\infty)$ always take a finite value larger than 0. The power-law model can be combined with the Bingham model to solve this. The Bingham model uses a yield stress τ_0 to model the apparent viscosity as a piecewise function [22, p. 116]. Since the Bingham model can not handle shear thinning and thickening behaviour, the same viscosity μ as in a Newtonian fluid is used. This model gives one section of the flow that behaves like a fluid and another that behaves like a solid. The yield stress τ_0 is used to decide at which shear stress τ the transition between the two phases happens. τ_{max} which is the maximum shear stress in any direction is used for this. The Bingham model is presented below:

$$\eta(\dot{\gamma}) = \mu + \frac{\tau_0}{|\dot{\gamma}|}, \quad \text{for} \quad \tau_{max} \geq \tau_0 \quad \text{and} \quad \dot{\gamma} \neq 0 \tag{7}$$

$$\eta(\dot{\gamma}) = \infty \quad \text{for} \quad \tau_{max} \leq \tau_0 \tag{8}$$

In order to combine the power-law model and the Bingham model, the Herschel Bulkley model is used which combines the piecewise velocity profile with the shear thinning/thickening behaviour [23, p. 13]. The Herschel Bulkley model is presented below:

$$\eta(\dot{\gamma}) = k|\dot{\gamma}|^{n-1} + \frac{\tau_0}{|\dot{\gamma}|}, \quad \text{for} \quad \tau_{max} \geq \tau_0 \quad \text{and} \quad \dot{\gamma} \neq 0 \tag{9}$$

$$\eta(\dot{\gamma}) = \infty \quad \text{for} \quad \tau_{max} \leq \tau_0 \tag{10}$$

The derivation of shear rate which is used in Herschel Bulkley model is carried out in Section 2.2.6. One problem with this model is that the value of $\eta(\dot{\gamma})$ becomes very large as $|\dot{\gamma}|$ approaches zero. In some cases, like a planar Poiseuille flow which is a two-dimensional flow between two plates, the shear rate $\dot{\gamma}$ will be equal to zero in the middle of the flow, leading to division by zero and an undefined apparent viscosity $\eta(\dot{\gamma})$. This is solved by using Papanastasiou Regularisation which combines Equations 9 and 10 into one continuous equation [24, p. 465]. this modified model is presented below:

$$\eta(\dot{\gamma}) = k|\dot{\gamma}|^{n-1} + \frac{\tau_0}{|\dot{\gamma}|}\left(1 - e^{-M|\dot{\gamma}|}\right) \tag{11}$$

Where the stress growth exponent M is the parameter that determines the transition between the two phases expressed in Equations 9 and 10. This parameter has no physical representation and can thus not be determined using any physical laws or equations. Instead, a suitable value has to be found through empirical methods.

2.2.5 Non-Dimensionalization

A brief introduction of non-dimensionalization procedure will be given here, while the details of this procedure can be found in literature [20, p. 274]. For a better understanding and being able to analyze the relationship between different physical quantities, it is convenient that the governing equation does not have any dimension. In order to do this some characteristic parameters are needed. The usual non-dimensionlization procedure generates well known dimensionless group such as Reynolds number (Re), Bingham number (Bn) and consistency (C). The Re describes a relation between the inertal and viscous forces in a flow. A low Re usually relates to a creeping laminar flow while a high Re usually relates to a turbulent flow [21, p. 23]. The Bn defines the ratio between yield stress and viscous stress. These number that represent dimensionless rheological properties will describe the physics of the flow, involve flow quantities such as characteristic length l_c, characteristic velocity v_c, characteristic kinematic viscosity ν_c, characteristic dynamic viscosity μ_c, and characteristic density ρ_c.

$$v_c = Re\frac{\mu_c}{\rho_c l_c} \tag{12}$$

$$\frac{\eta}{\mu_c} = \frac{k}{\mu_c}\Big(\frac{v_c}{l_c}\Big)^{n-1}\Big(\frac{l_c}{v_c}\Big)^{n-1}|\dot{\gamma}|^{n-1}\frac{\mu_c}{\rho_c l_c} + \frac{\tau_0}{\mu_c}\frac{l_c}{v_c}\frac{v_c}{l_c}\frac{1}{|\dot{\gamma}|}\Big(1 - e^{-M\frac{v_c}{l_c}\frac{l_c}{v_c}|\dot{\gamma}|}\Big) \tag{13}$$

Since l_c, $v_c > 0$, the equation can be written as:

$$\frac{\eta}{\mu_c} = \frac{k}{\mu_c}\Big(\frac{v_c}{l_c}\Big)^{n-1}\Big|\frac{l_c\dot{\gamma}}{v_c}\Big|^{n-1} + \frac{\tau_0}{\mu_c}\frac{l_c}{v_c}\frac{1}{\Big|\frac{l_c\dot{\gamma}}{v_c}\Big|}\Big(1 - e^{-\frac{Mv_c}{l_c}|\frac{l_c\dot{\gamma}}{v_c}|}\Big) \tag{14}$$

In order to make Equation 14 more compacted and readable, some parameters can be grouped into dimensionless rheological parameters as it is shown in Table 1 and using these parameters Equation 14 can be written as Equation 15.

Table 1: Defined dimensionless rheological parameters

Dimensionless parameter	Description
$\mathrm{C} = \frac{k}{\mu_c}\Big(\frac{v_c}{l_c}\Big)^{n-1}$	Dimensionless Consistency
$Bn = \frac{\tau_0}{\mu_c}\frac{l_c}{v_c}$	Bingham Number
$M^* = \frac{Mv_c}{l_c}$	Dimensionless stress growth exponent
$\dot{\gamma}^* = \frac{l_c\dot{\gamma}}{v_c}$	Dimensionless shear rate
$\eta^* = \frac{\eta}{\mu_c}$	Dimensionless apparent viscosity

$$\eta^*(\dot{\gamma}^*) = C|\dot{\gamma}^*|^{n-1} + \frac{Bn}{|\dot{\gamma}^*|}\Big(1 - e^{-M^*|\dot{\gamma}^*|}\Big) \tag{15}$$

Some of these characteristics parameters such as density and viscosity vary in a non-Newtonian fluid. In a fluid like blood, the viscosity varies between 0.003 and 0.04 Ns/m^2 in the overall human body [26]. However, when the flow physics are modelled assuming incompressible Newtonian fluid under steady state conditions, it is convenient that the characteristic viscosity can be set to 0.04 Ns/m^2, and characteristic density equal to 1000 kg/m^3 as a general value for the intracranial blood [26]. The characteristic length l_c, being the diameter of an artery, is taken $l_c = 3.08$ mm [26]. The Reynolds number is taken as $Re = 1$. Using above parameters the characteristic velocity can be calculated through Equation 12. Table 2 summarizes the characteristic values as well as n, k and τ_0 [26].

Table 2: Characteristics parameters

Parameters parameter	label	Description
Density	ρ_c	1000 kg/m^3
Viscosity	μ_c	0.004 Ns/m^2
Length/Mean diameter	l_c	3.08 mm
Reynolds number	Re	1
Yield stress	τ_0	0.04 N/m^2
Flow index	n	0.95
Consistency	k	$1.712.10^{-2} Ns^n/m^2$

2.2.6 Lattice Boltzmann method

The Lattice Boltzmann method (LBM) is an alternative way to solve the N-S equations. The LBM is appropriate for complex geometries and seems particularly effective for the simulation of flows in microsystems, where both mesoscopic dynamics and microscopic statistics are important [29]. The method solves a simplified Boltzmann equation, shown in Equation 16 on a discrete lattice. LB method is based on principles that are valid for gasses, but certain limitations are introduced to apply these principles in fluid dynamics. The essence of this method is solving a system of equations (Navier-Stokes equations) to obtain the resulting field of macroscopic physical quantities such as velocity, pressure and shear-dependent viscosity of the fluid by using a variable parameter related to the local shear rate

The main advantage of this method is that it is not necessary to solve the used differential equations of N-S, hence, the implementation is relatively simple and it is possible to parallelize the software based on LB method [31]. The LB equation reads as:

$$f_i(\mathbf{x} + \mathbf{e_i}\Delta x, t + \Delta t) - f_i(\mathbf{x}, t) = \Omega_i(\mathbf{x}, t) \tag{16}$$

The LBM consists of mainly two operations. Streaming on the left-hand side, and the collision operator on the right-hand side of the Equation 16. The collision operator represents the change of distribution function due to particle collision which can be written as below:

$$\Omega_i(\mathbf{x}, t) = \frac{-1}{\tau}\Big[f_i(\mathbf{x}, t) - f_i^{eq}(\mathbf{x}, t)\Big] \tag{17}$$

where τ is the relaxation time which is related to the kinematic viscosity ν as below:

$$\tau = \frac{6\nu + 1}{2} \tag{18}$$

and $f_i(\mathbf{x}, t)$ donates the density function along direction e_i at lattice position $\mathbf{x}$ and time t. $f_i^{eq}(\mathbf{x}, t)$ is the equilibrium form of the distribution function [29, 28].

Shear rate $\dot{\gamma}$ used in HB equation, is obtained as:

$$\dot{\gamma} = 2\sqrt{D_{II}} \tag{19}$$

$$D_{II} = \sum_{\alpha,\beta=1}^{l} S_{\alpha\beta} S_{\alpha\beta} \tag{20}$$

$$S_{\alpha\beta} = -\frac{3}{2\tau} \sum_{i} f_i^{(1)} e_{i\alpha} e_{i\beta} \tag{21}$$

where $S_{\alpha\beta}$ and D_{II} are strain rate tensor and the second invariant of the strain rate tensor respectively. The $f_i^{(1)}$ terms are usually calculated between two consecutive iterations and l is equal 3 as it is a 3 dimensional problem [28].

3 Method

In this chapter the method of this study is presented. The chapter is divided into three subsections; geometry reconstruction, the calculations needed to decide the bifurcation angles and finally simulation. This includes the investigation of the blood flow of the cerebral circulation system of two patients with the focus on the middle cerebral artery.

3.1 Geometry reconstruction

In order to be able to analyze the cerebral circulation system with CFD, the geometry of the brain needed to be reconstructed. Two different vascular trees were extracted from open-source MRI-scans. These scans were provided from two overall healthy people, that in this study are referred to as patient 01 and patient 27. MATLAB was used to process the MRI-scans, where they were made in to a binary 3D-matrix. Thresholding was used to extract the vascular tree from the rest of the brain. To extract the blood vessels the threshold constant was set to 210, where the areas with lower pixel intensity are set to the value zero. Those that are over 210 are set to one. To get a clear model unwanted small volumes were filtered out. The matrix was then plotted as a 3D-model. The 3D-model for patient 27 is shown in Figure 2, where the MCA is highlighted with a blue circle.

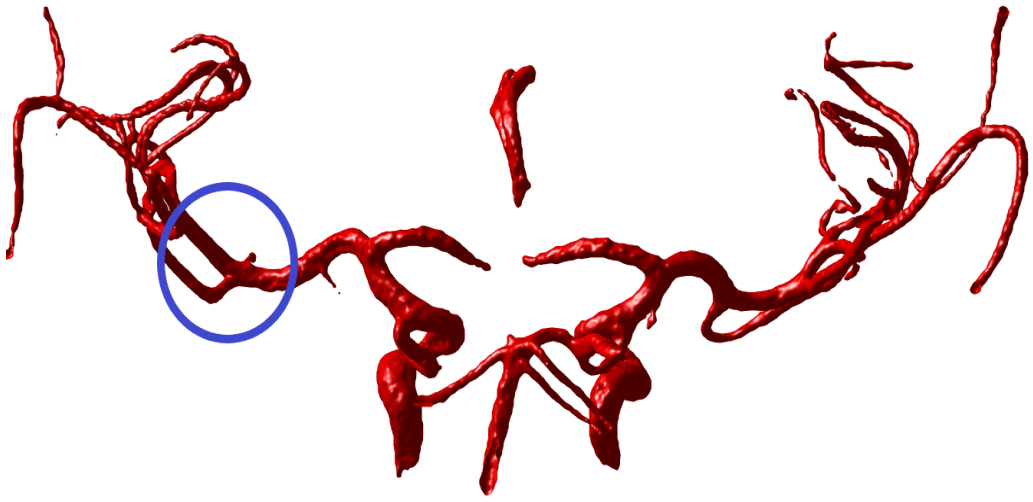

Figure 2: Part of the vascular tree for patient 27 reconstructed in MATLAB, where the blue circle shows the MCA [*ownimage*]

To select a suitable vessel for the simulation, the two 3D-models of the patients were compared. The selected vessel is the middle cerebral artery (MCA). Important aspects in this choice were that it was possible to identify that they were the same vessel for both the patients, with the common morphology for both patients with a superior and interior branching. There were also morphological differences as can be seen by comparing Figure 3 and Figure 4. The differences is important because

it shows how this can affect the flow through the artery. It was also chosen because of its bifurcation, since it is a significant element of brain morphology. Another important aspect is that the outflows and inflow of the vessels were in the same coordinate plane, as it is a requirement for facilitating the simulation. In Figure 3 it is shown how both the outflows and the inflows are in the YZ-plane for patient 01 and the same for patient 27 in Figure 4. The last reason is that the MCA is relatively exposed to intracerebral hemorrhage and aneurysms, and thereby making the analysis of this particular artery more relevant. To confirm that it was the right vessel that was taken out, Erik Lindgren, resident in Neurology at Sahlgrenska University Hospital in Gothenburg, was consulted. He confirmed that the vessel was the MCA for both patients and that they where comparable.

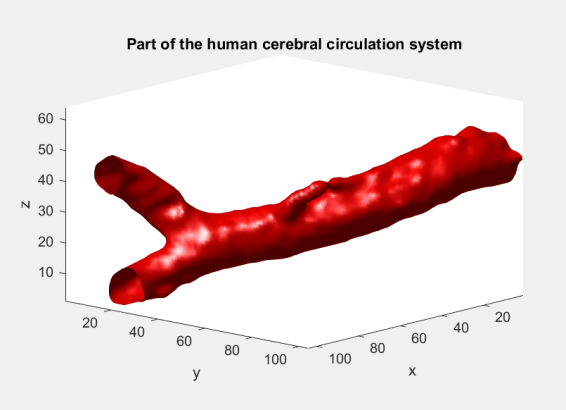

Figure 3: Middle cerebral artery of patient 01 reconstructed in MATLAB from MRI-scans[own image]

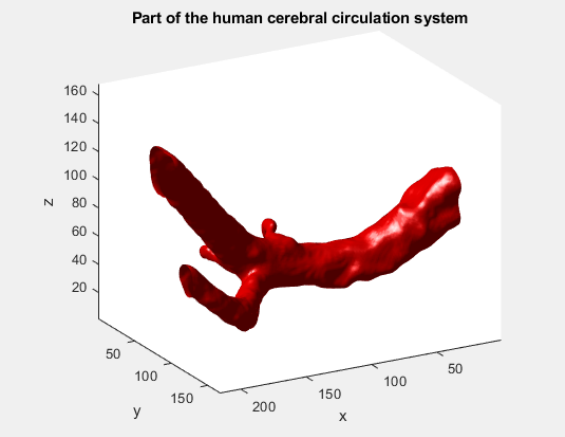

Figure 4: Middle cerebral artery of patient 27 reconstructed in MATLAB from MRI-scans[own image]

In order to simulate the flow, a buffert of blood had to be created at the inflow and the outflow to get a steady state flow in the artery. This was made by doing an extension of the box with the double length of the ordinary box.

3.2 Calculation of the bifurcation angles

In order to calculate the bifurcation angles of the two artieries, a MATLAB-code was written. The irregular geometry of the MCA requires some calculations in order to compute the angles. This calculation can be divided into three steps: determining the coordinates for the geometric centers along the artery, making regression lines for the points and finally bifurcation angle calculations.

Firstly the coordinates for the middle points were calculated from the 3D-matrix, where the points were taken out separately for the first branch and then after the bifurcation, for the superior and inferior part. The superior means the upper branch and inferior means the lower branch. The middle points of the artery were calculated by analyzing the YZ-surface with a step size of 20 in the x-direction for the first branch, and thus a new surface for every twentieth step. For the superior and inferior branches, a step size of five was chosen since they change more in a shorter x-distance. The

middle points were then calculated by taking the mean value in the y-direction for all points that contained a value greater than zero in that surface, and then the same for the z-direction. In order to control the calculations, the middle points were plotted in Figure 5. As can be seen in Figure 5, there had to be space at the bifurcation which couldn't be used when calculating the coordinates, due to the fact that there would have been to much interference between the branches.

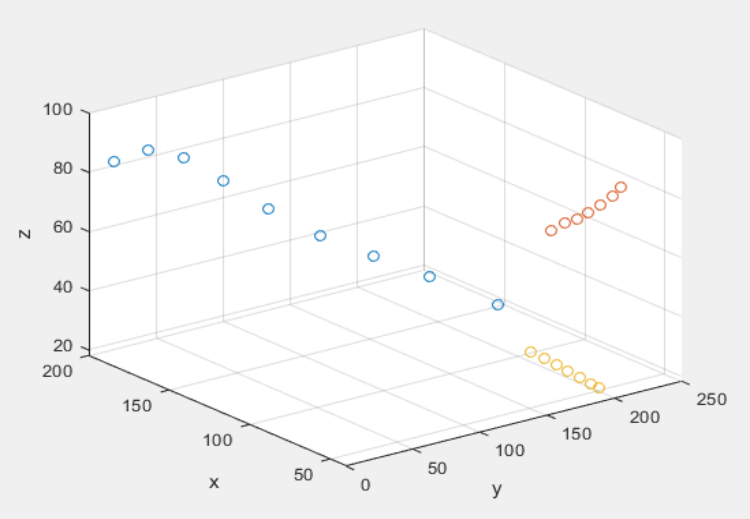

Figure 5: Coordinates for the geometric centers, with first branch in blue, superior in red and inferior in orange [own image].

By taking all the points for each branch, it was possible to do a linear regression. This to describe the otherwise irregular geometry in a regular and compact way, so that it can be used mathematically when calculating the angles. The linear regression was made by implementing a Principle components analysis (PCA) method i MATLAB, which had the purpose of minimizing the perpendicular distance from the coordinates to the regression line. Figure 6 shows the linear regression for patient 01, where the points are in blue and the regression line in black.

In order to calculate the angles, the origin of the coordinate system had to be moved to a point where the branches intersect. As can be seen in Figure 6, the regression lines had to be extended in order to see where the lines intersect. Since there is a 3D system, the lines do not cross, but if the lines are seen from a y view, an x view and a z view, they intersect in each 2D view. All three lines still do not cross the same point in the 2D-views. Thus, the mean of the intersection lines for each view were taken as the coordinates for the new origin. From the new origin, the three angles from each regression line to the next could be computed for each patient. They where listed as α, β and γ as in Figure 7.

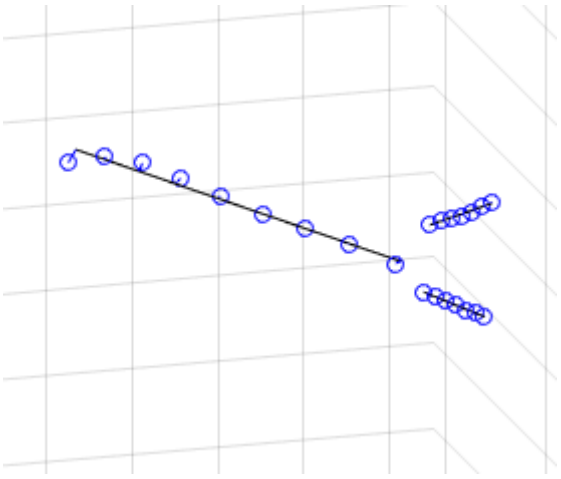

Figure 6: Linear regression for patient 01[own image]

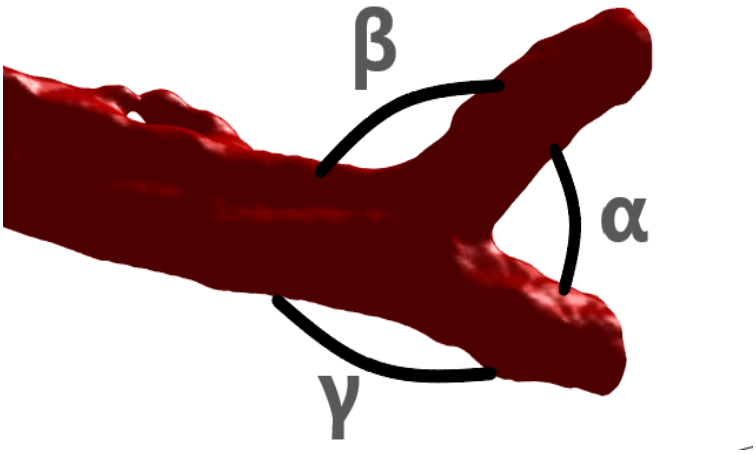

Figure 7: Angles α, β and γ was calculated for each MCA[own image]

3.3 Simulation

3.3.1 Simulation Parameters

The simulation that was used is based on the Lattice Boltzmann method that is described in Section 2.2.6 [27]. In order to properly run the simulation, some parameters for the flow and model needed to be calculated. These were then used as inputs for the simulation. The parameters that were calculated were mainly used to simulate the non-Newtonian behaviour of the fluid. The input parameters are expressed in Lattice Boltzmann units (LB units).

In order to convert physical units to LB units the dimensionless parameters first had to be calculated from physical units. A conversion from dimensionless parameters to LB units can then be done. This was done according to the theory described in section 2.2.5, using the characteristic parameters presented in Table 2. The characteristic velocity v_c was calculated first using Equation 12. This was then used to calculate the Bingham number Bn and the dimensionless consistency C according to Table 1

To calculate the parameters needed in LB units, some characteristic parameters in LB units were needed. These are characteristic length l_{LB}, characteristic density ρ_{LB} and characteristic viscosity μ_{LB}. In the simulation, the density is defined as $\rho_{LB} = 1$ and the viscosity as $\mu_{LB} = 1/6$. The characteristic length is calculated as the average diameter in LB units in the section of the artery before the bifurcation.

From this, the needed parameters were calculated. The pressure gradient $\frac{dp}{dl}$ for a pipeflow was calculated using the velocity v_{LB} and the flow rate Q_{LB}:

$$v_{LB} = Re\frac{\mu_{LB}}{\rho_{LB} l_{LB}} \tag{22}$$

$$Q_{LB} = v_{LB}\pi\frac{l_{LB}^2}{4} \tag{23}$$

$$\frac{dp}{dl} = 128\frac{\mu_{LB} Q_{LB}}{\pi l_{LB}^4} \tag{24}$$

The remaining parameters, the consistency k_{LB} and the yield stress $\tau_{0,LB}$ were calculated as:

$$k_{LB} = C\mu_{LB}\left(\frac{l_{LB}}{v_{LB}}\right)^{n-1} \tag{25}$$

$$\tau_{0,LB} = Bn\mu_{LB}\frac{v_{LB}}{l_{LB}} \tag{26}$$

Outside of these three parameters, two more were needed. The flow index n is given in Table 2 while a suitable value for the stress growth exponent M was produced in section 3.3.2

3.3.2 Validation of LBM

A validation of the Lattice Boltzmann Method was done to make sure that the parameters used in the simulation were accurate according to theory. In order to do this, a simplified case with a planar Poiseuille flow was used to make the simulations run faster which in turn made the validation more efficient, as well as making the analytical solutions easier to solve.

The stress growth exponent M, whose function is avoiding division by zero in the Herschel Bulkley model, should be chosen correctly. Figure 8 shows the velocity profile between the two walls for different choices of M. Starting from a high value, which results in a discontinuity close to the walls, and reducing it to a very low value which yields a large velocity in the center of the flow. M was chosen as $M = 500$ as this avoided the discontinuity which does not follow theory while also being as large as possible to minimize the correction for a vessel of this size.

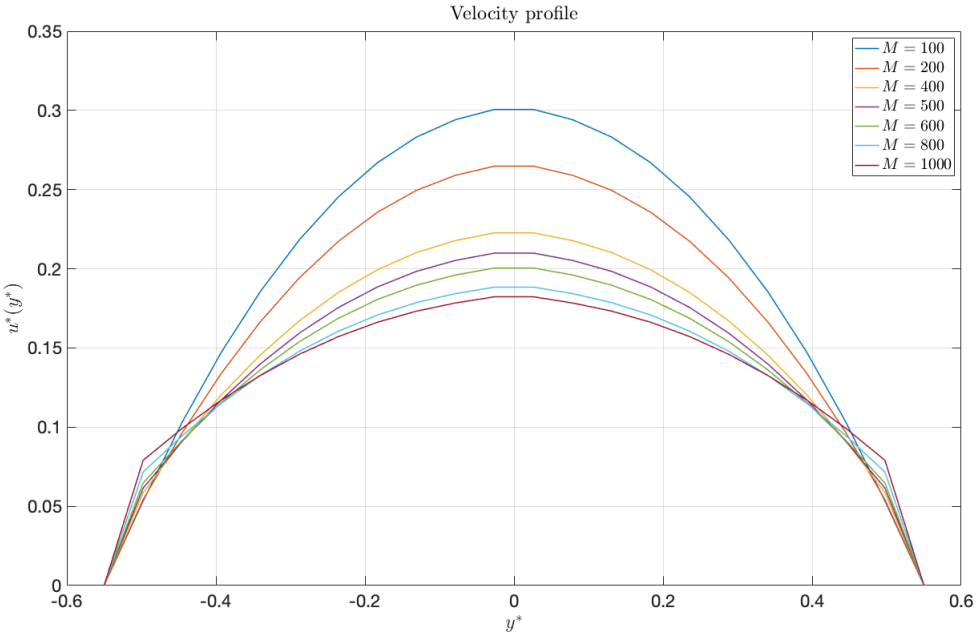

Figure 8: Velocity profile for planar Poiseuille flow with different choices for M [own image]

In order to validate that the other parameters worked as intended, a plot with four different velocity profiles retrieved from four simulations were used, which can be seen in Figure 9. The first profile, labeled as *Newtonian Flow* in the plot shows a Newtonian flow with a constant velocity, where the profile takes the form of a parable which is expected [21, p. 236]. For the next profile, labeled as *Separate Consistency and Viscosity*, separate values are used for consistency and viscosity according to the values expressed in Table 2. This flow does not follow any of the mentioned models since there is still no shear thinning or yield stress τ_0. Despite this, it is still a useful study to validate that the parameters used to model the non-Newtonian flow in the simulation has the desired effect. The third profile shows the flow with a shear thinning behaviour, $n = 0.95$. This flow is very similar to the previous one, which is because the velocity of the flow is not high enough for the shear thinning behaviour to properly affect the flow. The last profile shows a flow according to the model that was used in the final simulation. The velocity is even lower here, due to the effect of the yield stress τ_0. All of the velocity profiles look as expected according to theory.

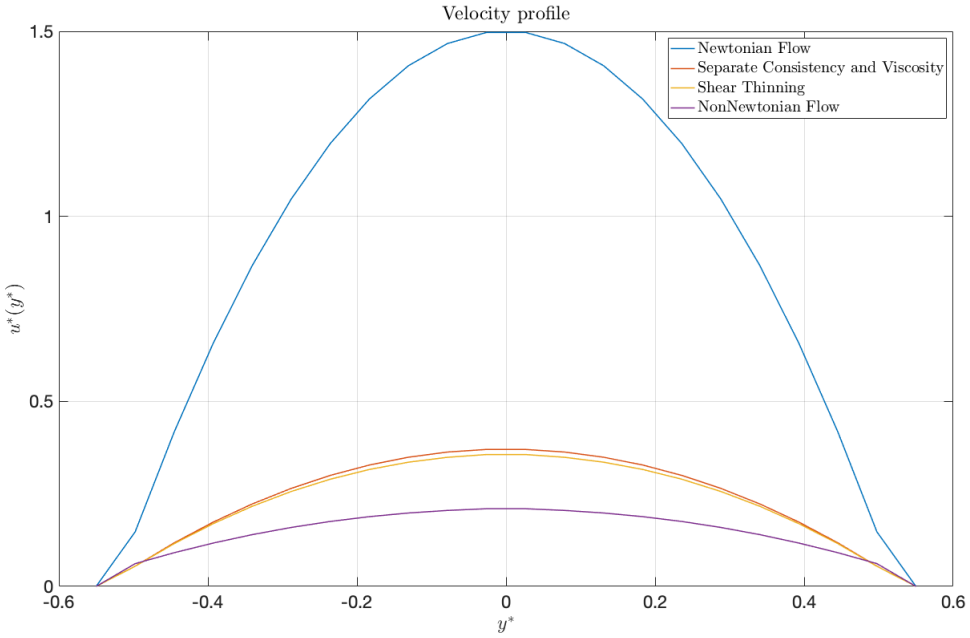

Figure 9: Velocity profiles for validation [own image]

To further validate that these velocity profiles look as expected, the profiles were calculated using another method, namely a numerical solution of the velocity profiles. This was done by numerically solving the Navier-Stokes equation, showed in Equation 2, using the apparent viscosity shown in Equation 11. The solver *bvp5c* was used in MATLAB, which is used to solve boundary value problems. These profiles along with the profiles gained from the simulations are shown in Figure 10. The data from the simulations are the same in Figure 9 as in Figure 10. It can be seen that the analytical solutions follow the simulations quite well. There is a difference in the *NonNewtonian flow*, which may be because *bvp5c* does not work well with such a mathematical formulation as the Herchel-Bulkley method used together with the Navier-stokes equation. Despite these differences,

it is still a good result that shows that the simulations follows the theory quite well. The following simulations are therefore valid according to what has been described in the theory in Section 2.

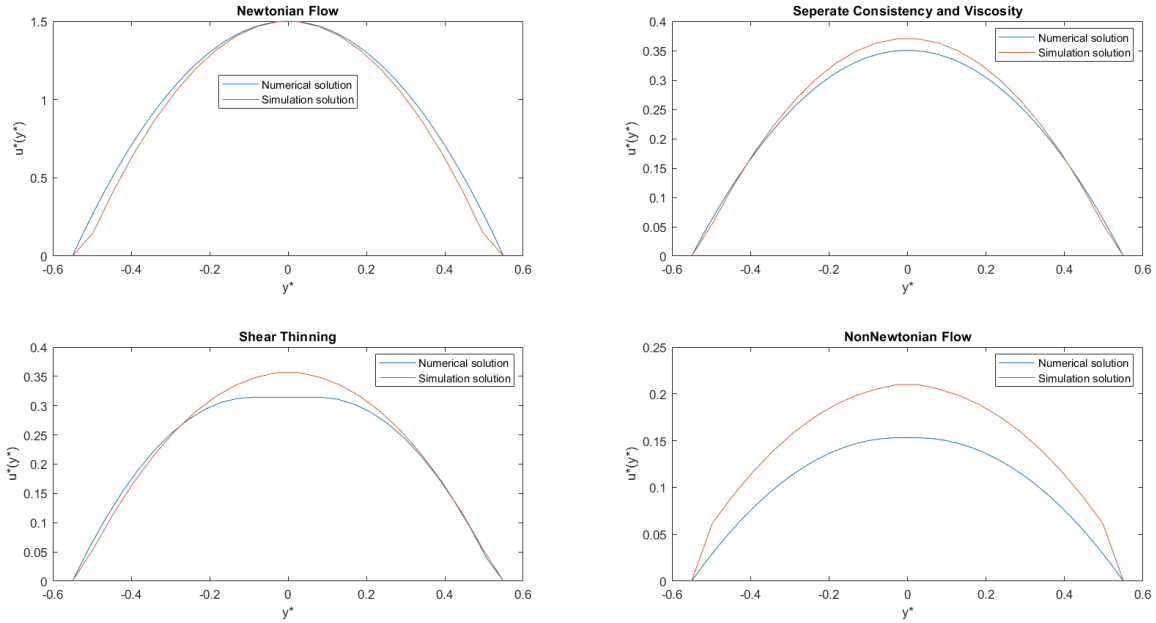

Figure 10: Velocity profiles for validation with both analytical and simulation solutions [own image]

3.3.3 Analysis of result

In order to visualize the results, which consisted of several 3D-matrices, two different types of plots were used. A number of slice plots were produced, showing the shear rate in each computational node for that particular slice. Due to the way the simulation outputs the results, the axes in the input and the output are not the same. The x-axis and y-axis are flipped in the output, compared to the input. The other plot shows the mean shear rate for all slices along the y-axis according to the coordinate system of the output.

In order to be able to analyze the results and compare it to the theory, the maximum shear rate in each slice plot was recalculated to dimensionless wall shear stress (WSS*) with Equation 27 by combining the dimensionless form of Equation 5 and Equation 11. The parameters k and τ_0 in Equation 27 were calculated using Equations 22-26.

$$WSS^* = \frac{\eta(\dot{\gamma})\dot{\gamma}}{\tau_0} = \frac{k\dot{\gamma}^n}{\tau_0} + (1 - e^{-M\dot{\gamma}}) \tag{27}$$

4 Result

The two simulations, one for each patient, ran for 10000 iterations each. Both simulations took a large amount of iterations to converge. The Reynolds number Re varied greatly for the first few thousand iterations and started to converge after 5000 iterations. The simulations were allowed to run for a further 5000 iterations to make sure that convergence had actually been reached. The Reynolds number has been plotted as a function of iterations, this is shown in Figure 11 for patient 01 and Figure 12 for patient 27. The pulsating behaviour seen in the graphs is due to the large buffer zones at the inlet and outlet together with a small amount of compressibility of the fluid.

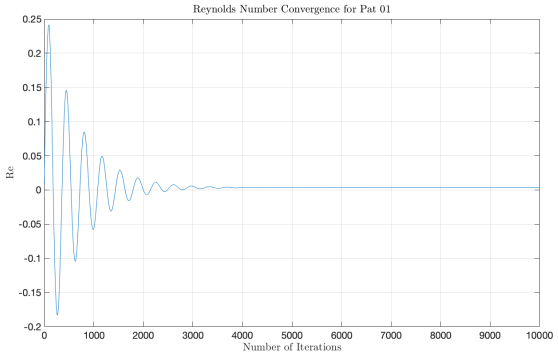

Figure 11: Reynolds number as a function of iterations for patient 01 [own image]

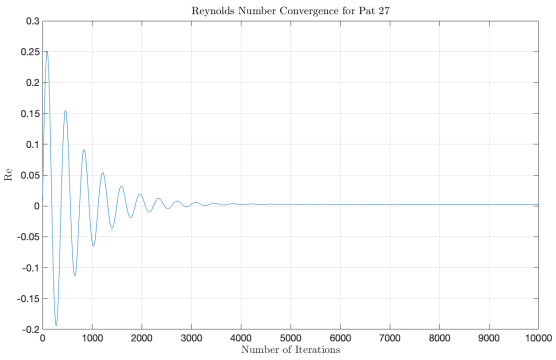

Figure 12: Reynolds number as a function of iterations for patient 27 [own image]

One way to analyze the results of the simulations is by looking at the shear rate $\dot{\gamma}$. The output from the simulations consists of several 3D-matrices containing data for all the pixels in the model. One of the matrices contains the shear rate for all computational nodes.

The mean shear rate $\bar{\dot{\gamma}}$ for each slice along the flow direction of the arteries were calculated and plotted in Figure 13. In this plot, the data has been non-dimensionalized in order to make the results for the two patients more comparable to each other. The two ends of the plot, roughly before 0.5 and after 4.5 characteristic lengths, are not as accurate as the rest of the plot due to the ends being close to the inlet. The low shear rate $\dot{\gamma}$ seen in these regions is due to this.

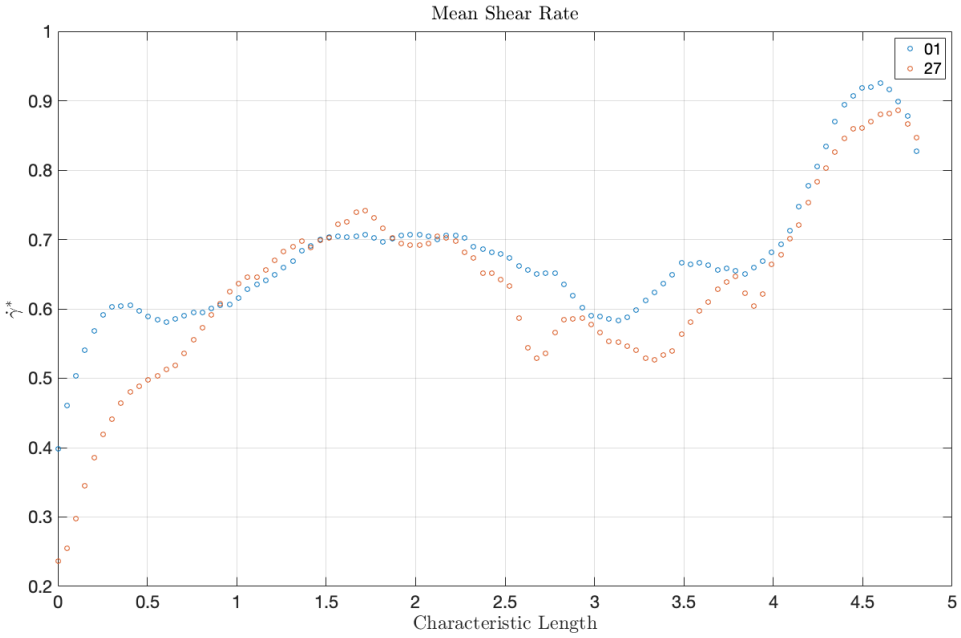

Figure 13: Dimensionless mean shear rate $\bar{\dot{\gamma}}^*$ along artery for both patients [own image].

It can be seen in Figure 13 that the mean shear rate $\bar{\dot{\gamma}}$ does not differ much between patients, except for a slightly higher overall shear rate $\dot{\gamma}$ in patient 01. For both patients there is a drop in shear rate $\dot{\gamma}$ around the bifurcation, roughly at $l_c = 3$ and a sharp upturn as the artery bifurcates. No analysis will be made regarding the flowstate after these upturns due to the flow being close to the outlets.

To further analyze the differences in shear rate $\dot{\gamma}$ between the two patients, several slice plots were made in different places along the artery for both patients. The plots show the shear rate $\dot{\gamma}$ in Lattice-Boltzmann units, and the values shown in the plots are therefore used to compare differences between the two patients, more than providing exact values for the actual shear rate $\dot{\gamma}$. In some of these plots there is a difference between the patients in where the slice has been placed along the y-axis. This is due to morphological differences. Two slices that are comparable have been chosen, regardless of where along the y-axis they have been placed. For example, two comparable plots has been placed at $y = 141$ for one patient and $y = 126$ for the other.

The first two plots, shown in Figure 14 for patient 01 and Figure 15 for patient 27, shows the shear rate $\dot{\gamma}$ before the bifurcation roughly halfway between the inlet and the bifurcation.

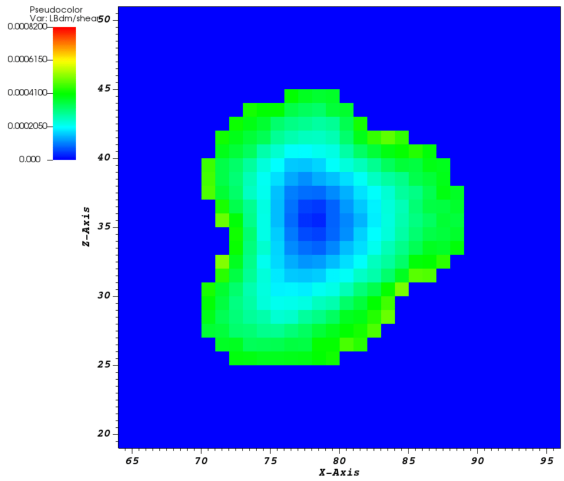

Figure 14: Slice-plot showing the shear rate $\dot{\gamma}$ at y=91 of artery before bifurcation in patient 01 [own image]

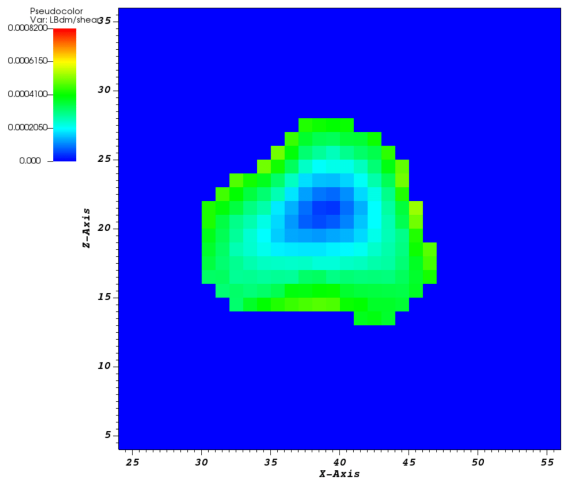

Figure 15: Slice-plot showing the shear rate $\dot{\gamma}$ at y=91 of artery before bifurcation in patient 27 [own image]

The flow in the two arteries has a very low or equal zero shear rate $\dot{\gamma}$ in the center of the artery. The two plots show that the shear rate $\dot{\gamma}$ is similar for the two patients, and that there is no region in either patient with a significant increase in shear rate $\dot{\gamma}$.

The next two slices, shown in Figure 16 for patient 01 and 17 for patient 27, show the shear rate $\dot{\gamma}$ when the artery has started to bifurcate.

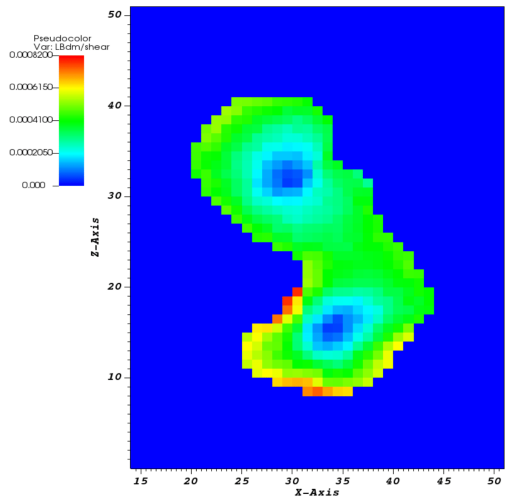

Figure 16: Slice-plot showing the shear rate $\dot{\gamma}$ at y=141 of artery at bifurcation in patient 01 [own image]

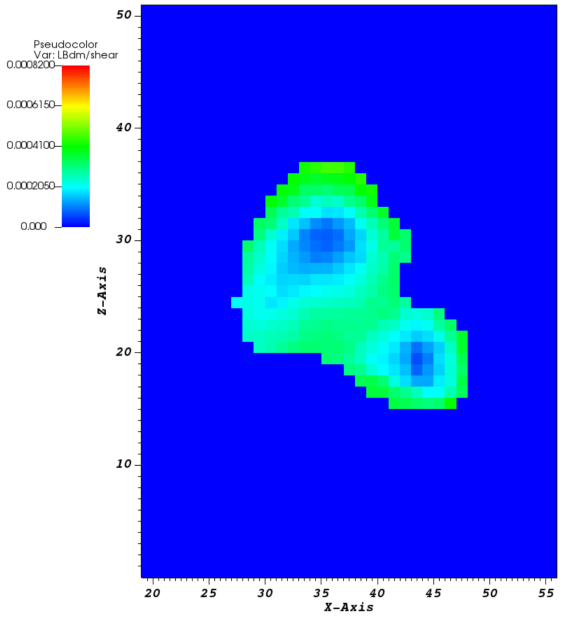

Figure 17: Slice-plot showing the shear rate $\dot{\gamma}$ at y=126 of artery at bifurcation in patient 27 [own image]

There is a clear difference in the magnitude of shear rate $\dot{\gamma}$ experienced by the two patients. For patient 01 there is a much higher shear rate $\dot{\gamma}$ in the inferior branch compared to rest of patient 01's slice as well as the slice for patient 27. Other than this spike in shear rate $\dot{\gamma}$ there is an overall higher intensity of shear rate $\dot{\gamma}$ for patient 01, as compared to patient 27, where the shear rate $\dot{\gamma}$ is even lower in the bifurcation than before the bifurcation.

The last two slices show the shear rate $\dot{\gamma}$ after the bifurcations. These are shown in Figure 18 for patient 01 and Figure 19 for patient 27.

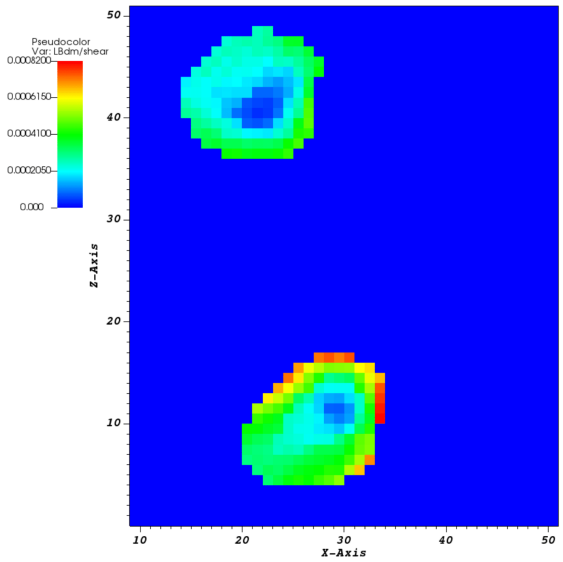

Figure 18: Slice-plot showing the shear rate $\dot{\gamma}$ at y=151 of artery after bifurcation in patient 01 [own image]

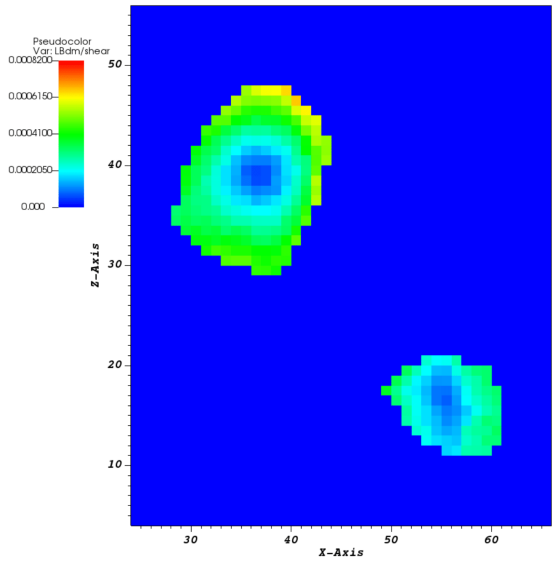

Figure 19: Slice-plot showing the shear rate $\dot{\gamma}$ at y=137 of artery at bifurcation in patient 27 [own image]

The heightened shear rate $\dot{\gamma}$ in the inferior branch in the bifurcation continues even after the bifurcation. The shear rate $\dot{\gamma}$ is as high or even higher after the bifurcation than in the bifurcation for patient 01. In patient 27 there is also a higher shear rate $\dot{\gamma}$, here it is in the superior branch, although not as high as for patient 01.

The γ angle for Patient 01 is in comparison to the other angles large with its 162.3 degrees. It is not far from 180 degrees which means that it does not change direction that much, it instead let the flow go kind of straight. This can also be seen when looking at the 3D-model of the MCA, see Figure 3, where the main branch and the inferior is almost aligned. It can also be seen in Table 3 that the difference in WSS* is much greater for patient 01 than for patient 27. As the γ-angle is the angle between the inferior and the main branch, see Figure 7 in section 3.2, there can be a correlation between the angle and the increase in WSS*. Moreover, the WSS* for patient 27 is relatively even and in the bifurcation and it has the same maximum for both parts. An interesting result is that the WSS* is lower there then before the bifurcation, to then get the a higher WSS* in superior after they split. The angles between the main part and the branches, β and γ, do not differ by more than 16 degrees, which is not much. Furthermore, the angle between the superior and inferior is only 40 degrees which is less than for patient 01 where the α-angle is 66 degrees. What one have to keep in mind is that the angles are calculated for the branches in relation to each other so the angles do not say in which plane they are offset, but only how they are offset relative to each other.

Table 3: Angles and shear rate for each patient

	Branch type	**Patient 01**	**Patient 27**
Angles [deg]	α Superior and inferior	66.0	40.0
	β Superior and main	129.6	112.5
	γ Inferior and main	162.3	128.7
Maximum local wall shear stress*	Before bifurcation	0.4533	0.4697
	In bifurcation	0.6660 (inferior)	0.4129 (in both)
	After bifurcation	0.6916 (inferior)	0.5698 (superior)

5 Discussion

In this chapter, the hemodynamic parameters from the simulation results are discussed in relation to the bifurcation angles of the MCA in the two patients. Moreover, sources of error along with future research is discussed. The last part of this chapter contains an analysis of societal and ethical aspects.

5.1 Morphology in relation to hemodynamic parameters

In the simulations, both the mean shear rate as well as the local shear rate in slice plots placed at different distances along the y-axis were produced. The mean shear rate was relatively similar in both patients, with an overall sligthly higher shear rate for patient 01. The small drop in shear rate in both patients around the bifurcation followed by a rise just after, aligns well with the theory in section 2.1.1. The main reason to the increase is that the bifurcation forces the fluid to a rapid decrease in velocity, causing kinetic energy to convert into pressure energy. The increased pressure itself implies a rise in wall shear stress, which leads to a higher shear rate according to Equation 5. Furthermore, the small reduction in shear rate just as the bifurcation starts to form, is mainly due to the fact that the surface where the velocity is distributed becomes larger. This will cause a reduction of the mean shear rate since the gradient goes to zero for very large surfaces. Thus, the reduction mainly depends on the increased surface of the slice. Since the model used in the simulation is not as accurate near the inlet and outlet respectively, no conclusion can be drawn about the flowstate in these regions. The overall higher mean shear rate in patient 01 can exist due to morphological differences. However, since the difference variates along the artery and are relatively small, potential sources of error in both the modeled used as well as in the geometry reconstruction need to be considered. A more detalied analysis of these areas will be covered in section 5.2.

Since the results from the local shear rates differed more than the mean shear rate, the slice plots provide an opportunity to analyze the results from a morphological perspective. By converting the maximum values of the shear rate in each plot, the potential correlation between high hemodynamic stresses due to morphology variations and stroke, becomes more distinguishable. Hence, the maxi-

mum local shear rates in the slice plots in Figure 12-13 are expressed as maximum local WSS* in Table 3. However, the relationship in Equation 5 remains accurate, which is assumed to be known in the coming analyzes of the slice plots. Every slice plot in Figure 12-17 contains a region in the center with a lower shear rate than at the artery walls, which aligns with the Bingham model. As seen in Figure 14 and Figure 15, there are no significant peaks in shear rate before the bifurcation. Moreover, Table 3 shows that the maximum WWS* is almost identical in the two patients with a just an insignificantly higher value in patient 27.

When analyzing Figure 14 and Figure 15, the middle of the bifurcation, a more interesting result is observed. Patient 01 has a higher overall shear rate than patient 27, with peaks that exceed the maximum WSS* in patient 27 by about 0.2531 units according to Table 3. Additionally, the inferior branch of patient 01 contains the largest shear rate and WSS*, while patient 27 has a fairly even distribution. Table 3 also shows that the α-angle is 22° larger than for patient 27. As suggested in chapter 2.1.1, some studies have provided the same result of a larger bifurcation angle leading to a higher hemodynamic stress. Another observation in Table 3 is that the superior branch in patient 01 has an offset to the main branch (β), which is lower than γ. In patient 27 however, β and γ are more similar, which seems to align with the fact that patient 27 has a more even shear rate distribution in the bifurcation. Patient 01 has a higher value in the inferior branch, which can be explained by the fact that γ is close to 180°. This implies that the inferior branch is more aligned with the main branch, and thus the preferred path of the fluid will be the inferior branch when bifurcating. It can also be explained in principle with the velocity vector. In the bifurcation, the velocity vector of the fluid divides into two directions; one superior and one inferior part. Since the vector component in the direction of the inferior branch is more aligned with the main branch, it will be bigger than the component in the direction of the superior branch. Hence, the shear stress and thereby shear rate will be higher in the inferior branch according to Equation 4.

Lastly, Figure 16 and 17 are analyzed. As seen in both Table 3 and Figure 16 and 17, the post-bifurcation slices provide the highest maximum WSS* for both patients. This aligns with the plots for the mean shear rate, Figure 11, as well as the explanation regarding the previously described convertion between kinetic and pressure energy. It is also higher than in the middle of the bifurcation, which is due to the reasoning about the velocity gradient in relation to the vessel surface. For patient 01, the highest shear rate and WSS* still occurs in the inferior branch as expected. However, a new peak in shear rate and thereby WSS* can be detected in the the superior branch for patient 27. According to Table 3, there is a slightly smaller offset for β than γ, which means that the higher shear rate and WSS* would be in the inferior branch similiar to patient 01 according to this reasoning. The reason to why this is not the case, is that the superior branch has a significantly larger diameter than the inferior, which implies that most of the blood will flow in this branch after the bifurcation, leading to a decreased diameter in comparison to the main branch. Consequently, a higher pressure, shear stress and shear rate will be obtained in the superior branch than in the inferior branch.

To summarize, the simulation results from both the mean shear rate as well as the local shear rate in different slices, seem to be well aligned with the theory provided in section 2. Furthermore, it is clear that patient 01 has higher peaks of WSS* in and after the bifurcation than patient 27. Thus, the results from this study alone implies that the morphology of patient 01 is less favorable when it comes to risk assessment of IA and other conditions that can cause stroke, since the hemodynamic stress is higher both in and after the bifurcation according to Table 3. The largest contributor to the increase in WSS* seems to be the magnitude of the bifurcation angle α, where a larger angle leads to a higher hemodynamic stress. However, since the angles only are calculated for the branches in

relation to each other, no conclusions can be drawn regarding if it matters in which direction the branches are offset.

5.2 Sources of error and future research

The results of this study implies that a larger bifurcation angle α is a part in developing IA and intracerebral hemorrhage, by causing higher hemodynamic stresses. Even though previous studies have as mentioned suggested the same conclusion, there are many sources of error and simplifications that need to be considered when evaluating the results.

Regarding the geometry, the fact that only two patients were considered is a clear limitation. Moreover, the variations between the two patients were limited to angles and sizes by excluding trifurcations and branching into smaller parts. The calculation process of the angles in the geometry also has room for improvement, since manual methods were used and implemented in MATLAB. Preferably, a software could have been used for a more precise result.

In the model used for the simulation, simplifications and approximations were made in order to reduce complexity. Some of these simplifications were assumptions on solid artery walls instead of elastic, as well as only simulating a steady state-flow without pulsation.

In order to further develop the usage of CFD for simulating the cerebral blood flow, a large number of more extensive studies need to be made. By trying to remove as many of the above described simplifications and sources of error as possible, the results will be more reliable. Hopefully, this study can be the start of a new beginning when using *in silico* methods for neurology research, and thus contribute to making progress within the preventive work against strokes.

5.3 Societal and ethical aspects

When dealing with people and lives it is always an important ethical aspect in who carries the responsibility for the methods accuracy. So for example, in this study, some simplifications was required which as previously described need further developments. This in order for the method to be accurate enough to be used on a regular basis in the medical field. The point of this is that the accuracy needs to be very high, which require more researchers in the field. In the future, it can also be a legal question in how big part of the doctors assessment the method should take, should this method be what decide operation or should other aids also be included in the assessment.

This method requires a collection of information about the patient, which also makes it a question of data security and personal integrity. This can be viewed with respect to two groups, firstly the group of people needed to do the researches of this method, and then the second group which is the patients who use this method when it is developed. Especially for the first group, it is very important that it can be followed up how the method works. This requires extensive information over time, which can make it hard to be anonymous.

6 Conclusion

The results of the study on the two patients aligns well with the suggested theory provided by previous studies that have been made on the MCA. A larger bifurcation angle, α, seems to impact the hemodynamic stresses in a non-desirable way by increasing them. Patient 01 has a higher overall shear rate and WSS* as well as higher peaks of local WSS* than patient 27, which seems to be caused by the fact that patient 01 has a larger bifurcation angle α than patient 27. Since previous research suggests this as one of the risk factors for developing IA and other conditions that can lead to stroke, the morphology and the bifurcation angles appear to be relevant factors to include in the preventive work against strokes. Furthermore, since the validation provided a reasonable result that was well aligned with the analytical solutions, it is fair to claim that CFD and the LBM based on this study can be used to simulate the cerebral blood flow. With additional research within the area, the possibilities of using *in silico* methods like LBM could lead to tremendous progress in the medical field and prevention of strokes.

7 References

[1] K. Kwaw, "Epidemiology of stroke", 1996, [online], https://www.ncbi.nlm.nih.gov/pmc/articles/PMC486569/pdf/jnnpsyc00010-0007.pdf, Accessed on: 2022-04-15

[2] "stroke", 1177, 2020-02-11, [online], https://www.1177.se/sjukdomar–besvar/hjarna-och-nerver/stroke-och-blodkarl-i-hjarnan/stroke/5, Accessed on: 2022-04-01

[3] O. Tanweer, T. A. Wilson, E. Metaxa, H. A. Riina1 and H. Meng, Journal of Cerebrovascular and Endovascular Neurosurgery 2014, vol. 16, no. 4, pp. 335-349, Dec. 2014, https://doi.org/10.7461/jcen.2014.16.4.335, Accessed on: 2022-04-15

[4] J. Xiang et al., "Hemodynamic–Morphologic Discriminants for Intracranial Aneurysm Rupture", 2011, [online]. https://www.ahajournals.org/doi/pdf/10.1161/strokeaha.110.592923, Accessed on: 2022-04-15

[5] S. P. Parker, *McGraw-Hill Dictionary of Scientific and Technical Terms*, 6th ed., New York, USA: McGraw-Hill, 2003.

[6] P. Morris et al., "Computational fluid dynamics modelling in cardiovascular medicine", 2015. [online] https://heart.bmj.com/content/102/1/18.short, Accessed on: 2022-04-10

[7] T. Wu and Q.Zhu, "Advancement in the haemodynamic study of intracranial aneurysms by computational fluid dynamics", 2020, [online]. https://www.sciencedirect.com/science/article/pii/S2589238X20300747?via

[8] R.Cammack, T.K.Attwood, P.N.Campbell, J.H.Parish, A.D.Smith, J.L.Stirling, F.Vella, Oxford Dictionary of Biochemistry and Molecular Biology, 2nd ed., Uk, Oxford University Press, 2006, [Ebook], Available: https://app.knovel.com/kn/resources/kpODBMBE01/toc?b-q=in%20silicob-content-type=dictionary%2Cencyclopediaincludesynonyms=noissueid=kt008O74KL

[9] J.Daintith, E.Martin, Dictionary of Science, 6th ed., UK, Oxford University Press, 2010, [Ebook], Available: https://app.knovel.com/kn/resources/kpDSE00001/toc?b-q=in%20vivob-content-type=dictionary%2Cencyclopediaincludesynonyms=noissueid=kt007X78Z1hierarchy=undefined

[10] C. K. Aidun, J. R. Clausen,"Lattice-Boltzmann Method for Complex Flows", 2010, [online]. https://www.annualreviews.org/doi/abs/10.1146/annurev-fluid-121108-145519, Accessed on: 2022-04-05

[11] Henry Knipe, "Middle cerebral artery", radiopaedia, [online]. 2021-12-21, https://radiopaedia.org/articles/middle-cerebral-artery, Accessed on: 2022-04-05

[12] Zhang, Wei et al. "Morphological parameters of middle cerebral arteries associated with aneurysm formation",National libary of medicine, 2021, [online]. https://pubmed.ncbi.nlm.nih.gov/32814989/, Accessed on: 2022-04-10

[13] D. Orozco and J. Sánchez-Manso. *Neuroanatomy, Middle Cerebral Artery*, 2021-06-26,[online], https://www.ncbi.nlm.nih.gov/books/NBK526002/, Accessed on: 2022-04-10

[14] J. Huang, W. Yang, "Treatment of middle cerebral artery (MCA) aneurysms: a review of the literature",2015, [online], https://cnjournal.biomedcentral.com/articles/10.1186/s41016-015-0001-8, Accessed on: 2022-04-10

[15] W. Kaspera, K. Ćmiel-Smorzyk, W. Wolański, E. Kawlewska, A. Hebda, M. Gzik, P. Ładziński, "Morphological and Hemodynamic Risk Factors for Middle Cerebral Artery Aneurysm: a Case-Control Study of 190 Patients", 2020, [online], https://www.nature.com/articles/s41598-019-56061-2

[16] S. Takeuchi, T. Karino, "Flow patterns and distributions of fluid velocity and wall shear stress in the human internal carotid and middle cerebral arteries", 2010, [online], https://www.sciencedirect.com/science/article/abs/pii/S0090301909002869

[17] F. Tütüncü, S. Schimansky, M. I. Baharoglu, B. Gao, D. Calnan, J. Hippelheuser, M. G. Safain, A. Lauric,A. M. Malek, "Widening of the basilar bifurcation angle: association with presence of intracranial aneurysm, age, and female sex", 2014, [online],https://thejns.org/view/journals/j-neurosurg/121/6/article-p1401.xml, Accessed on: 2022-05-02

[18] "Thresholding", Federal Agencies Digital Guidance Initative, [online]. https://www.digitizationguidelines.gov/term.php?term=thresholding, Accessed on: 2022-04-06

[19] M. J. Simmonds, H. J. Meiselman, and O. K. Baskurt, *Blood rheology and aging*, National libary of medicine, 2013, [online]. https://www.ncbi.nlm.nih.gov/pmc/articles/PMC3796705/, Accessed on: 2022-04-05

[20] L. Lanotte et al, "Red cells' dynamic morphologies govern blood shearthinning under microcirculatory flow conditions," *Proceedings of the National Academy of Sciences*, vol. 113, nr 47, Nov. 2016, https://doi.org/10.1073/pnas.1608074113, Accessed on: 2022-04-17

[21] F. M. White, *Fluid Mechanics*, 8th ed, New York, USA: McGraw-Hill Education, 2016

[22] F. Irgens, *Rheology and Non-Newtonian Fluids*, Cham, Switzerland: Springer International Publishing Switzerland, 2014, [Online] Available: https://link.springer.com/book/10.1007/978-3-319-01053-3, Accessed on: 2022-05-05

[23] R. Byron-Bird, G.C. Dai and B. J. Yarusso, "THE RHEOLOGY AND FLOW OF VISCOPLASTIC MATERIALS," *Reviews in Chemical Engineering*, vol. 1, nr. 1, pp. 1-70, 1983, doi:10.1515/revce-1983-0102

[24] G. R. Burgos, A. N. AAlexandrou, V Entov, "On the determination of yield surfaces in Herschel–Bulkley fluids," *Journal of Rheology vol. 43*, nr.3,pp. 463-483, 1999 doi:10.1122/1.550992

[25] E. Chalhoub, S. Dellås, L. Sparks, J. Stenmark, M. Svensson and G. Vallbo, "Computational Fluid Dynamics of Human Cerebral Circulation Systems: A Fluid Mechanic Perspective," B.S. Thesis, Department of Mechanics and Maritime Sciences, Chalmers University of Technology, Gothenburg, Sweden, 2021.

[26] L. Forsman, A. Mudarres, I. Nilsen, E. Svensson, S. Talal A. von Sydow, "Computational Fluid Dynamics of Human Cerebral Circulation Systems: A biological perspective," B.S. Thesis, Department of Mechanics and Maritime Sciences, Chalmers University of Technology, Gothenburg, Sweden, 2021. [Online]. Available: https://hdl.handle.net/20.500.12380/303577

[27] D. Maggiolo (2016), lbdm [Source Code], https://gitlab.com/dariom/lbdm

[28] J. Boyd, J. Buick and S Green, "Journal of Physics A: Mathematical and General A second-order accurate lattice Boltzmann non-Newtonian flow model," *Journal of Physics A: Mathematical and General*, vol. 39, no. 46, Nov 2006, https://doi.org/10.1088/0305-4470/39/46/001

[29] J. Tu, G. H. Yeoh and C. Liu, *Computational Fluid Dynamics: A Practical Approach*, 3rd ed., Oxford, UK: Butterworth-Heinemann, 2019. [Online]. Available: https://doi.org/10.1016/C2015-0-06135-4, Accessed on: 2022-05-10

[30] S. Kandlikar, S. Garimella, D. Li, S. Colin, M. R. King, *Heat Transfer and Fluid Flow in Minichannels and Microchannels*, 2nd ed., Oxford, UK: Butterworth-Heinemann, 2014. [Online]. Available: https://doi.org/10.1016/C2011-0-07521-X, Accessed on: 2022-05-10

[31] N. Filipovic, *Computational Modeling in Bioengineering and Bioinformatics*, Cambridge, USA: Academic Press, 2020. [Online]. Available: https://doi.org/10.1016/C2017-0-03417-1, Accessed on: 2022-05-10

DEPARTMENT OF
MECHANICS AND MARITIME SCIENCES
CHALMERS UNIVERSITY OF TECHNOLOGY
Gothenburg, Sweden 20xx
www.chalmers.se

CHALMERS
UNIVERSITY OF TECHNOLOGY